Dalton Transactions

ROYAL SOCIETY OF CHEMISTRY

PAPER

View Article Online
View Journal

Cite this: DOI: 10.1039/d5dt01689d

SMM behaviour in a $\{Co^{III}_4Co^{II}_2Dy^{III}_2\}$ complex: Co(II)-based thermal barrier and Dy(III) spectator role

Lara Martinez,[a] David Hunger,[b] Carlos Cruz, [c,d] Joris van Slageren, [b] Verónica Paredes-García [c,d] and Pablo Alborés *[a]

Received 17th July 2025,
Accepted 18th September 2025

DOI: 10.1039/d5dt01689d

rsc.li/dalton

We report the synthesis, structure, and magnetic properties of a novel Co/Dy heterometallic complex, $[Co^{III}_4Co^{II}_2Dy^{III}_2(tea)_4(CH_3COO)_4(OH)_2(NO_3)_4]\cdot 2H_2O$ (**1**), the first structurally characterized example of a mixed-valent $\{Co^{III}_4Co^{II}_2Dy^{III}_2\}$ motif. It comprises two butterfly-like $\{Co^{III}_2Co^{II}Dy^{III}\}$ units linked by carboxylate and alkoxide bridges. X-ray diffraction shows unique Dy(III) and Co(II) sites, with Dy(III) nine-coordinated and Co(II) in a rhombic tetrahedral geometry. Magnetic data and quantum chemical calculations reveal weak Co(II)–Co(II) antiferromagnetic exchange, negligible Co(II)–Dy(III) interactions, and moderate Co(II) zero-field splitting ($D \approx 12$–20 cm^{-1}), which drives single-molecule magnet behavior below 14 K. AC studies indicate multiple tunneling pathways and an Orbach barrier ($U_{eff} \approx 65$ cm^{-1}) arising from Co(II), while Dy(III) ions remain largely magnetically decoupled.

Introduction

Single-molecule magnets (SMMs) are recognized as molecular materials exhibiting slow relaxation of magnetization at low temperatures due to a combination of low-lying energy magnetic levels together with significant anisotropy.[1,2] Since their discovery, SMMs have been extremely attractive due to their potential applications in areas such as high-density information storage, spin-based electronics, quantum computing and low-temperature magnetic refrigeration.[3–7] Unlike bulk magnetic materials, SMMs retain magnetic bistability at the molecular level, making them ideal candidates for future technologies based on molecular-scale information processing.[3]

Among the various strategies developed to enhance the performance of SMMs, the incorporation of both 3d and 4f metal ions to build up coordination complexes has proven particularly promising.[8,9] These 3d–4f heterometallic systems combine the favorable characteristics of both metal families: the relatively strong exchange interactions of 3d transition metals and the large magnetic anisotropy (due to strong angular momentum contribution) of 4f lanthanide ions. Importantly, the synergistic magnetic behavior emerging from 3d–4f interactions can eventually suppress the undesirable quantum tunneling of magnetization (QTM), which is a limiting factor in achieving high performance SMMs.[8,10–14]

In this context, complexes containing Co(II) and Dy(III) ions have emerged as particularly attractive candidates for developing high-performance SMMs.[15] Co(II), a Kramers ion ($S = 3/2$), can exhibit significant single-ion anisotropy, especially in distorted octahedral, trigonal bipyramidal and also in tetrahedral environments, where large axial zero-field splitting (ZFS) parameters (D) are observed.[16–18] On the other hand, the Dy(III) ion, also a Kramers ion, ($^6H_{15/2}$) possesses a high magnetic moment and intrinsic Ising-type anisotropy, arising from its strongly oblate electron density and large total angular momentum ($J = 15/2$), making it one of the most widely studied lanthanides in SMM research.[19,20] In contrast to 3d–4f systems where the 3d ion is magnetically isotropic such as Cr(III)/Dy(III), the Co(II)/Dy(III) combination offers a mixture of two highly anisotropic metal types leading to a system with enhanced magnetic anisotropy.

A key factor influencing SMM behavior in 3d–4f heterometallic assemblies is the magnetic exchange interaction between the metal centers. Although 4f–4f interactions are generally weak due to the core-like nature of 4f orbitals, the presence of bridging ligands connecting 3d and 4f centers can promote the more effective 3d–4f exchange coupling. This interaction can play a key role in quenching QTM as was observed for example in several Cr(III)/Dy(III) systems.[10,21–23] In the case of anisotropic Co(II) ion in combination with Dy(III) ion, the geometry and symmetry of the coordination environment are critical for aligning the anisotropy axes of both metal ions, a prerequisite for enhancing the expected SMM behaviour.[24–27]

[a]Departamento de Química Inorgánica, Analítica y Química Física/INQUIMAE (CONICET), Facultad de Ciencias Exactas y Naturales Universidad de Buenos Aires, Pabellón 2, Ciudad Universitaria, C1428EHA Buenos Aires, Argentina. E-mail: albores@qi.fcen.uba.ar; Fax: +5411/4576-3341
[b]Institute of Physical Chemistry, University of Stuttgart, Pfaffenwaldring 55, Stuttgart, Germany
[c]Departamento de Ciencias Químicas, Facultad de Ciencias Exactas, Universidad Andres Bello, Avenida República 275, Santiago de Chile, Chile
[d]Centro para el Desarrollo de la Nanociencia y Nanotecnología, CEDENNA, Santiago, Chile

Searching through the structurally characterized reported Co/Dy SMMs, it is found that only a few Co(II)–Dy or Co(II)Co(III)Dy mixed-valence heterometallic (*i.e.* at least one Co(II) present) SMMs have been reported up to now. The reason of this observation is that Co(II) can be easily air oxidized under open atmosphere reaction conditions. The reported Co(II) containing Co/Dy heterometallic SMMs include $\{Co^{II}Dy\}$,[28] $\{Co^{II}_2Dy\}$,[29] $\{Co^{II}_2Dy_2\}$,[30] $\{Co^{II}_2Dy_{10}\}$,[31] $\{Co^{III}_2Co^{II}Dy\}$[32] and $\{Co^{III}_4Co^{II}_2Dy_4\}$[33] motifs. It is evident that this family of complexes is still a fertile research field.

With this background in mind, we have extended our previous work on Co/Dy SMMs based on pivalate and aminoalcohol ligands,[34–39] exploring reaction with acetate and triethanolamine (H_3tea) ligands (Scheme 1). We have been able to isolate and structurally characterize a new complex with formula $[Co^{III}_4Co^{II}_2Dy^{III}_2(tea)_4(CH_3COO)_4(OH)_2(NO_3)_4]\cdot 2H_2O$ (**1**). In addition to complex **1**, to the best of our knowledge, there are only other two reported complexes with the motif $\{Co_6Dy_2\}$ both baring all Co(II) ions.[40,41] However, complex **1** is the first example of a polynuclear Co/Dy system with the $\{Co^{III}_4Co^{II}_2Dy_2\}$ motif.

We have studied DC and AC magnetometry response of complex **1**, as well as X-band and HF-EPR spectra. With the aid of quantum computations we are discussing the SMM behaviour in the new reported complex.

Results and discussion

Synthesis and structural characterization

The reaction of a mixture of Co(II) and Dy(III) nitrates in the presence of triethanolamine ($teaH_3$) and acetate (CH_3COO^-) ligands at room temperature and employing acetonitrile as solvent afforded complex **1**. The partial oxidation to a Co(II)/Co(III) combination most probably arises due to atmospheric oxygen oxidation as already observed in related complexes containing alcohol–amine ligands like $teaH_3$.[38]

Complex **1** crystallizes in the $P\bar{1}$ triclinic space group, with half a molecule and two acetonitrile solvents in the asymmetric unit due to the inversion centre. The latter splits the complex molecular structure of **1** into two equivalent $\{Co^{III}_2Co^{II}Dy^{III}\}$ units covalently linked by *syn–anti* μ_2-CH_3COO and μ_2-OR (from the tea^{3-} ligand) bridges (Fig. 1).

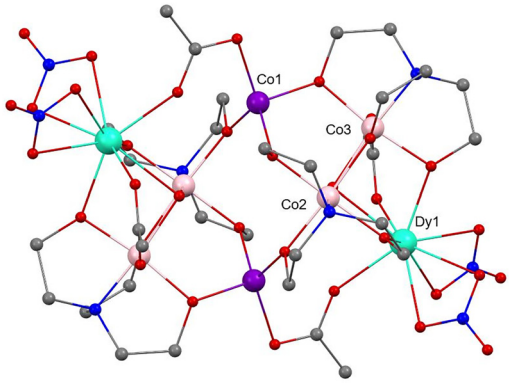

Fig. 1 Ball and stick X-ray structure molecular representation of complex **1**. Hydrogen atoms as well as atoms of disorder components have been omitted for sake of clarity. Co(III): pink; Co(II): violet; Dy: green; O: red; N: blue; C: gray.

Each $\{Co^{III}_2Co^{II}Dy^{III}\}$ moiety can be described as an asymmetric butterfly-type structure with the dimeric $\{Co^{III}_2(tea)_2(OH)\}$ motif in the body position and the Co(II) and Dy(III) sites at both wings. The $\{Co^{III}_2\}$ unit is connected to the Dy(III) site through multiple bridges involving μ_2-OR (tea^{3-}), μ_3-OH and μ_2-*syn*,*syn*-CH_3COO^-. The Dy(III) coordination sphere is further completed with two κ^2-nitrate ligands and the *syn–anti* μ_2-CH_3COO^- bridge to the Co(II) site of the other $\{Co^{III}_2Co^{II}Dy^{III}\}$ moiety. On the other hand, the connection of the $\{Co^{III}_2\}$ unit to the other butterfly wing, the Co(II) site, occurs exclusively through two μ_2-OR bridges from the tea^{3-} ligand. The coordination sphere of the Co(II) site is completed by the *syn–anti* μ_2-CH_3COO^- bridge to the Dy(III) site and the μ_2-OR (tea^{3-}) bridge to one of the Co(III), both other $\{Co^{III}_2Co^{II}Dy^{III}\}$ moiety. Overall, complex **1** can be described as two equivalent asymmetric butterfly $\{Co^{III}_2Co^{II}Dy^{III}\}$ cores tiled through the butterfly body with Dy(III) wing sites pointing to opposite sides (Fig. S1). To the best of our knowledge, **1** is the third structurally characterized example of a complex with $[Co_6Dy_2]$ core exhibiting this novel topology. In fact, the other previously reported examples lack Co(III) ions,[40,41] being complex **1** the first $[Co_6Dy_2]$ mixed valent Co(II)/Co(III) complex.

Focusing on the local environment at each symmetry independent metal site, the Dy(III) shows a nine-coordination sphere, which according to the CShM values[42] is geometrically

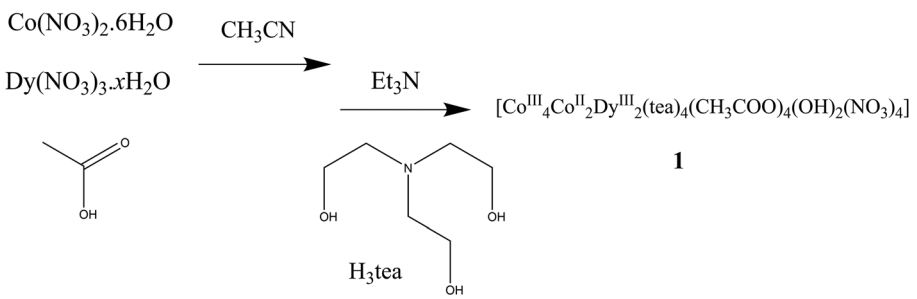

Scheme 1 Preparation of complex **1**.

close to a Muffin (1.842) like structure or alternatively to a capped square antiprism, CSAP (1.853) (Fig. S2). The Dy–O bond distances range between 2.230(3) and 2.528(6) Å, with a mean value of 2.416(4) Å. The shortest bond involves an alkoxide group of the tea^{3-} ligand (the one opposite to the μ_2-*syn–anti*-CH_3COO^- bridge), while the longest corresponds to one of the nitrate ligand oxygen atoms.

The Co(II) site (Co(1)) shows a distorted tetrahedral coordination environment, (CShM, 1.240), with three shorter Co–O bonds, 1.946(4), 1.949(4) and 1.964(4) Å (–OR group of tea^{3-}) a longer one, 2.024(4) Å (μ_2-*syn–anti*-CH_3COO^- bridge). Additionally, the O–Co–O angles show two near to ideal 108.8(2)° and 109.6(2)° values and the other two deviating to 100.9(2)° and 125.9(2)° values and involving the μ_2-*syn–anti*-CH_3COO^- bridge. The distortion of the ideal tetrahedral geometry points to a vacant trigonal bipyramid (vTBP) (or triangular pyramid), in fact the CShM value for this latter ideal geometry is 1.968, not so far from the CShM value for the tetrahedron one. The distance of the Co(II) site to the basis of the triangular pyramid is *ca.* 0.4 Å. Hence, the Co(II) site can alternatively be described as a highly distorted tetrahedron or a vacant trigonal bipyramid one (Fig. S2).

Finally, the Co(III) sites of the butterfly body core, show as expected for this ion, slightly distorted octahedral coordination spheres (CShM values of 0.563 (Co2) and 0.485 (Co3)). The Co–O bond distances span 1.871(4)–1.952(4) Å (Co2) (mean value: 1.906(4) Å) and 1.884(5)–1.933(3) Å (Co3) (mean value: 1.906(4) Å); while the unique Co–N bond lengths are 1.903(5) (Co2) and 1.903(4) (Co3) (Fig. S2).

The metal–metal distances within the butterfly moieties are Dy(III)–Co(III): 3.2545(7) Å (Co3), 3.4208(9) Å (Co2); Co(III)–Co(II): 3.306(1) Å (Co3), 3.312(1) Å (Co2); Dy(III)–Co(II): 5.6522(9) Å and Co(III)–Co(III): 2.924(1) Å (Fig. S3). On the other hand, the inter-butterfly ligand bridge mediated metal–metal distances are: Dy(III)–Co(II), 4.2088(9) Å (μ_2-*syn–anti*-CH_3COO^- bridge) and Co(II)–Co(III), 3.4925(9) Å (μ_2OR bridge tea^{3-}). Finally, the intra-molecular Co(II)–Co(II) and Dy(III)–Dy(III) distances, not directly mediated by ligand bridges are 4.8809(9) Å and 8.6890(7) Å, respectively (Fig. S3).

A double intra-molecular H-bond is found between both butterfly moieties that involve the hydroxide and tea^{3-} alkoxide groups (Fig. S4). Complex **1** is packed in the crystal structure through C–H···O interactions that involve the tea^{3-} and the nitrate ligands of neighbour molecules, while acetonitrile solvent molecules are also showing C–H···O and C–H···N interactions with neighbour complex **1** molecules (Fig. S5). As a result, the closest metal–metal intermolecular distances are Co(II)···Co(II), 6.422(1) Å; Co(II)···Co(III), 7.206(1) Å; Dy(III)···Co(III), 7.8452(8) Å, Dy(III)···Co(II), 8.8274(9) Å and Dy(III)···Dy(III), 8.4819(7) Å. Except for the Dy(III)···Dy(III) distance that notably is very close to the inter-molecular value, all the other distances are much longer than the intra-molecular ones (Fig. S6).

Magnetic properties: experimental and quantum chemical calculations

From a magnetic point of view complex **1** behaves as a $\{Co^{II}_2Dy^{III}_2\}$ unit, due to the closed-shell nature of Co(III) ions. In this sense, a square arrangement is envisioned with only Dy(III)–Co(II) (from different butterfly moieties) direct bridging through a (μ_2-*syn–anti*-CH_3COO^- bridge) (Fig. 2).

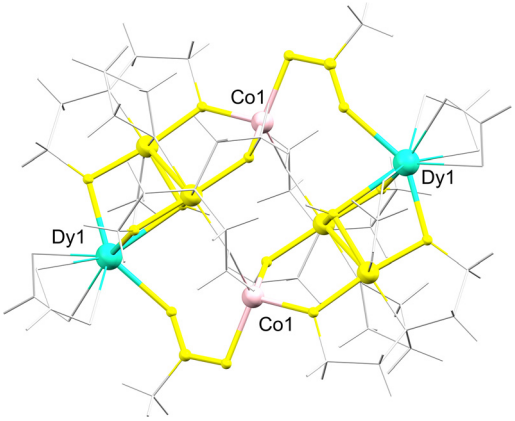

Fig. 2 $\{Co^{II}_2Dy^{III}_2\}$ magnetic core in complex **1** molecular structure. Yellow atoms correspond to the bridging pathways.

To further elucidate the magnetic behaviour of complex **1** we performed DC and AC magnetometry as well as EPR measurements with quantum computations as a supporting tool.

DC magnetic data

The χT value of 31.2 cm^3 K mol^{-1} observed for complex **1** at room temperature is in excellent agreement with the expected value for two isolated Co(II) ions (S = 3/2, g = 2, 1.87 cm^3 K mol^{-1}) and two completely uncoupled Dy(III) ions (J = 15/2, gJ = 4/3, 14.2 cm^3 K mol^{-1}) of 32.1 cm^3 K mol^{-1}. Upon lowering temperature, χT values smoothly decrease down to *ca.* 100 K, followed by a more pronounce decreasing to reach a final value of 24.1 cm^3 K mol^{-1} at 2 K (Fig. 3). This high value at 2 K indicates that magnetic states are considerably populated at this temperature. The decrease in χT with decreasing temperature is attributed to the continuous depopulation of excited crystal field states towards lower temperatures. The effect is far too strong to be attributed to the exchange interactions, which structural data suggest should be weak.

The isothermal magnetization represented as reduced magnetization data at low temperatures further supports the previous analysis, with not saturating neither superimposing isotherms. Moreover, a sigmoidal feature above 40 kOe is observed at 2 K data, characteristic of a level crossing (Fig. 3). The maximum reduced magnetization value reached at the maximum applied field and lowest temperature is about 16$N\mu$, which agrees with the expected value for two isolated Co(II) ions (S = 3/2, g = 2, 3$N\mu$) and two isolated Dy(III) ions with m_J = 15/2 ground doublet (m_J = 15/2, g_J = 4/3, 5$N\mu$) (Fig. 3).

Due to the strong anisotropic nature of Dy(III) ion, understanding these DC magnetometry data from a simple spin Hamiltonian modelling is impossible. Thus, we performed quantum computations as an alternative tool: we used BS-DFT calculations for obtaining isotropic exchange interaction strengths and SA-SOC-CASSCF to obtain the low-lying energy

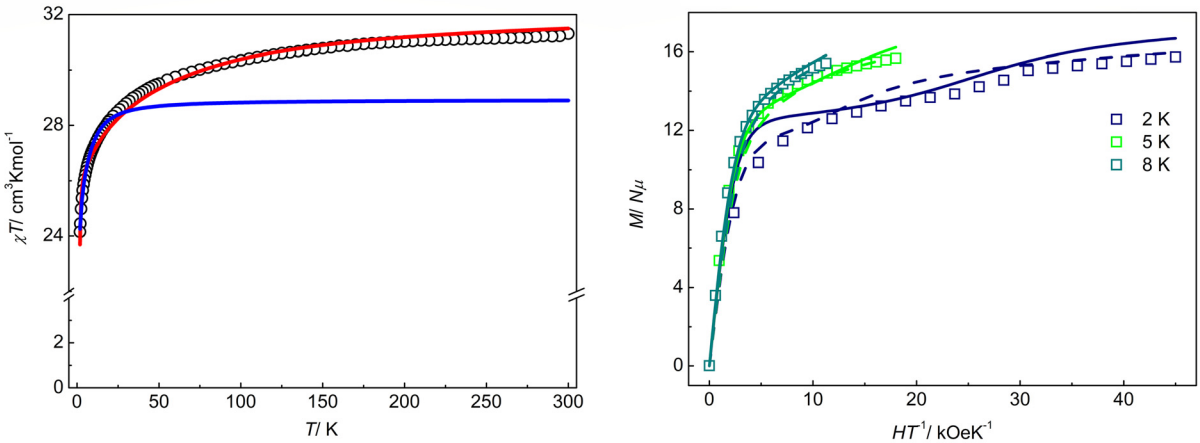

Fig. 3 Left: χT *vs.* T plot of complex **1** at 1000 Oe in the 2–300 K range. Open symbols: experimental; full lines: simulated with POLY_ANISO routine without any exchange interaction (red); simulated with best fitting parameters according to spin Hamiltonian described in the text and below 40 K (blue). Right: Reduced magnetization of complex **1** up to 90 kOe. Open symbols: experimental; full lines: simulated with best fitting parameters according to the spin Hamiltonian described in the text (dashed line: g values fixed to quantum computed values).

level structure of the single ions as well as their respective g-tensor values for each Kramers doublet (Tables 1 & 2).

As already discussed, looking at the metal sites topology in complex **1**, a very weak Co(II)–Co(II) exchange interaction is expected as no ligand through bridging is present (Fig. 2). The Co(II) sites are only connected *via* closed-shell Co(III) ions and at *ca.* 4.9 Å distance (*cf.* structural section). BS-DFT computed value is $J_{\text{Co–Co}} = -0.4$ cm^{-1}, which is small for a 3d–3d exchange interaction, in agreement with *a priori* expectation. On the other hand, Co(II)–Dy(III) exchange is also expected with a low value, as is usually found for 3d–4f exchange interactions. In this case, both metal sites are directly bridged by a *syn–anti* μ_2-acetate connection. The computed value for the isotropic contribution is $J_{\text{Co–Dy}} = -0.13$ cm^{-1}. Hence, the scenario for complex **1**, as previously suggested, is one with weak exchange interactions, at least considering the quantum computation results. This should afford a non-isolated ground state with several low-lying excited states.

Regarding single ion quantum computations, the unique symmetry-independent highly distorted tetrahedral Co(II) ion, shows an $S = 3/2$ with moderate zero-field splitting contribution and a high rhombic distortion. Computed values are: $g = \{2.41, 2.34, 2.20\}$ ($g_{\text{iso}} = 2.32$); $D = 14$ cm^{-1} and $|E/D| = 0.18$. The description with a spin-only model with ZFS Hamiltonian term seems appropriate as the third excited doublet is at *ca.* 2600 cm^{-1}. The ground Kramers doublet (KD) affords a g tensor with following values: $g_{\text{GS}} = \{2.00, 3.37, 5.93\}$, while the first excited doublet at *ca.* 30 cm^{-1} above shows the following g tensor: $g_{\text{KD1}} = \{1.15, 1.29, 6.40\}$. The ground KD g tensor is oriented along the C_3 axis of the vTBP geometry of Co(II) site (*cf.* structural section) which is coincident with the bond between Co(II) and one of the tea^{3-} alkoxide O atom (Fig. S7).

Table 1 Experimental and quantum computed magnetic parameters

		Experimental	
	Quantum computed	DC magnetometry	EPR
$J_{\text{exc Co–Co}}$/cm^{-1}	−0.40	−1.4 −1.0/−0.6 (fixed g values)	−0.3 (X-band) −0.2 (HF)
$J_{\text{exc Co–Dy}}$/cm^{-1}	−0.13	—	—
$J_{\text{dip Co–Co}}$/cm^{-1}	-9.3×10^{-4}	—	—
$J_{\text{dip Co–Dy}}$[a]/cm^{-1}	1.9×10^{-2}	—	—
$J_{\text{dip Dy–Dy}}$[a]/cm^{-1}	-3.8×10^{-2}	—	—
g_{Co} ($S = 3/2$)x, y, z (g_{iso})	2.41, 2.34, 2.20 (2.32)	2.11	1.86, 1.95, 1.71 (X-band) 2.02 (iso, X-band) 2.08/2.77/1.66 (HF) 2.18 (iso, HF)
D_{Co}/cm^{-1}	14.4	>7 18/−16 (fixed g values)	12
$\|E/D\|_{\text{Co}}$	0.18	—	0.15 (X-band) 0.14 (HF)
$g_{\text{eff Dy}}$ GKD/x, y, z ($g_{\text{eff,iso}}$)	0.04, 0.08, 19.7 (11.4)	12.4	—

[a] Computed with $S_{\text{eff}} = 1/2$ (GKD, Dy(III)).

Table 2 Quantum computed single ion magnetic parameters of the lowest KDs

Dy(III)					Co(II)			
E/cm^{-1}	g_x	g_y	g_z		E/cm^{-1}	g_x	g_y	g_z
0.0	0.04	0.08	19.71	97% m_J = 15/2	0.0	2.00	3.37	5.93
124.6	1.20	2.87	14.81	75% m_J = 13/2	30.1	1.15	1.29	6.40
179.3	0.17	3.21	13.65		2643.6	1.21	2.14	6.69
246.5	5.21	5.34	9.08		2761.8	1.84	2.14	4.85
293.5	0.94	3.03	11.81		3643.2	0.19	0.21	7.03
355.3	1.48	2.43	13.73					
421.5	0.29	0.42	16.65					
541.3	0.05	0.10	19.38					

With respect to the unique symmetry independent Dy(III) site, the ground KD is essentially a pure m_J = 15/2 state (97%) with an axial g tensor, g_z = 19.71 and transversal components g_x = 0.04 and g_y = 0.08. The first excited KD is at 125 cm^{-1} (75% m_J = 13/2, g_z = 14.8, g_x = 1.2, g_y = 2.9). The ground m_J = 15/2 state was already anticipated from the reduced magnetization data. The ground KD g-tensor is aligned very close to the shortest Dy–O bond (the one that involves the tea^{3-} alkoxide O atom) making an angle of *ca.* 14° (Fig. S7). The overall splitting into the eight KDs of the J = 15/2 ground state of the Dy(III) ion due to symmetry lowering is of *ca.* 540 cm^{-1}. From these quantum computed results, the ground KD g-tensor of Dy(III) site makes an angle of *ca.* 36° with the ground KD g tensor of the Co(II) site bridged by the *syn–anti* μ_2-acetate, hence they exhibit non-collinearity (Fig. S7).

A possible attempt to model the DC-magnetometry data employing the *ab initio* single-ion results is through the POLY_ANISO routine that relies on the Lines approximation to the exchange interactions.[43,44] However, this approach is not successful in this case as it is not possible to properly account for the magnetization data profile. The non-Ising nature of Co(II) ground KD maybe the reason of the failing of Lines approximation. On the other hand, the χT *vs.* T data profile can be properly modelled employing the *ab initio* results for single Co(II) and Dy(III) sites and completely neglecting any exchange or dipolar interaction (Fig. 3). This becomes a further proof that the exchange interaction is weak and only affecting DC magnetometry data at the lowest temperatures, in this case, the reduced magnetization data.

Considering the quantum computed single ions low energy levels, the simplest approach to tackle the magnetization DC data modelling is the following spin Hamiltonian:

$$\hat{H} = \left(g_{\mathrm{Co}} \sum_{i=1,1'} \hat{S}_{\mathrm{Co}_i} + g_{\mathrm{eff,\,Dy}} \sum_{i=1,1'} \hat{S}_{\mathrm{eff,\,Dy}_i} \right) \mu \vec{B} + D \sum_{i=1,1'} \left(\hat{S}^2_{z\mathrm{Co}_i} - \frac{5}{4} \right) - 2J_{\mathrm{Co-Co}} \hat{S}_{\mathrm{Co}_1} \hat{S}_{\mathrm{Co}_{1'}} \quad (1)$$

where the Co(II) ions are described as S = 3/2 with a single ion ZFS contribution, and Dy(III) ions as the isolated ground KD with its corresponding effective g-tensor. As already discussed, of all possible operative exchange interactions, the strongest one is only considered. Additionally, to avoid overparameterization and despite the Ising nature of Dy(III) ground KD, an isotropic g_{eff} value was employed. A very good data fitting (employing PHI package[45]) is achieved with the following parameters: g_{Co} = 2.11; $g_{\mathrm{eff,\,Dy}}$ = 12.4; $J_{\mathrm{Co-Co}}$ = −1.4 cm^{-1} and D > 7 cm^{-1} (Fig. 3). The D parameter cannot be unequivocally established, but a lower bound is set (Fig. S8). If a negative D parameter is forced, unreasonable g parameters are obtained. This outcome, together with quantum computations supports a positive value for the Co(II) site D parameter. The value found for the $g_{\mathrm{eff,\,Dy}}$ parameter is slightly above the maximum expected isotropic value of 11.5 (for g_z = 20 and $g_{x,y}$ = 0). Alternatively, the isotropic g values can be fixed to the *ab initio* computed ones, in this case the best fitting parameters reached are: g_{Co} (fixed) = 2.32; $g_{\mathrm{eff,\,Dy}}$ (fixed) = 11.4; $J_{\mathrm{Co-Co}}$ = −1.0 cm^{-1} and D = 18 cm^{-1} or $J_{\mathrm{Co-Co}}$ = −0.6 cm^{-1} and D = −16 cm^{-1}. In this case the value of the D parameter is better defined (with no possibility of sign distinction (Fig. S9)), suggesting a mean value close to the quantum computed one. With respect to the Co(II)–Co(II) exchange interaction parameter, the experimental values found with the different fitting approaches are also in good agreement with the BS-DFT computed value (Table 1).

Any attempt to include the Co(II)–Dy(III) interaction in the model ends in overparameterization and indeed affords a negligible value for this parameter. Some explanation is needed at this point, as the BS-DFT computed value for $J_{\mathrm{Co-Dy}}$ shows that it should be at same magnitude order than $J_{\mathrm{Co-Co}}$. If the BS-DFT value is correctly predicting this parameter magnitude order, one possible explanation of its negligible experimental value can be found in the dipolar interaction contribution to the overall isotropic exchange value. In fact, the *ab initio* computed value for the isotropic component of the Co(II)–Dy(III) dipolar interaction is positive in sign, hence it can compensate the negative contribution of the exchange interaction (Table 1). It can be shown, to further support the idea of a negligible Co(II)–Dy(III) interaction, that the reduced magnetization data profiles are completely dominated by the Co(II)–Co(II) exchange interaction in the presence of the strong single ion ZFS contribution (Fig. S10).

Even if the Co(II)–Co(II) exchange interaction cannot be extracted from the DC susceptibility data, the low temperature region is correctly reproduced with eqn (1) Hamiltonian and the best fitting parameters arising from magnetization data

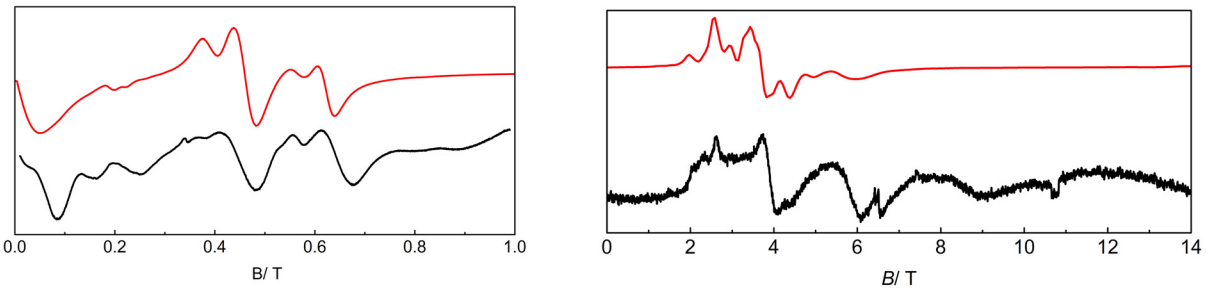

Fig. 4 Powder EPR spectra of complex **1**. Left: X-band at 7 K; right: 180 GHz at 5 K. Black line: experimental; red line: simulated; linewidths = 2.2 GHz (left) and 30 GHz (right) (see text).

fitting (Fig. 3). According to *ab initio* single ion Dy(III) computations, the first excite KD it only starts being populated above 40 K, thus it is expected that susceptibility data below this temperature can be reproduced by the above-mentioned modelling.

EPR data

The powder X-band EPR spectrum collected at 7 K of **1**, shows several broad resonances in the whole range up to 800 mT, with three leading ones at *ca.* 80 mT, 500 mT and 700 mT (Fig. 4). It is possible to simulate these main features considering eqn (1) Hamiltonian. Notably, the spectrum appears dominated only by the Co(II) sites. In fact, a Hamiltonian like the one in eqn (1), but without the inclusion of Dy(III) sites term it is enough to reproduce experimental data.

The parameters governing the EPR spectrum profile are the D and $|E/D|$ ZFS terms and the Co(II)–Co(II) isotropic exchange interaction (Table 1). The g-tensor components can hardly be distinguished, with alternative similar simulations choosing an isotropic g tensor, an anisotropic one or taking as fixed values the quantum computed g-tensor components. The other parameters arising from the X-band EPR spectrum simulations are: D = 12 cm^{-1}; $|E/D|$ = 0.15 and J_{CoCo} = −0.3 cm^{-1}, in good agreement with magnetometry DC data as well as quantum computed results. No information about Dy(III) g-tensor neither Dy(III)–Co(II) interaction is outcoming from X-band EPR data.

We achieved also high-frequency (HF) EPR spectra at 5 K within 180 and 350 GHz on the same powder sample. Again, broad resonances between 2–8 T are observed which become severely broaden at increasing frequency (Fig. S11). The best resolved HF-EPR spectrum is observed at the lowest frequency of 180 GHz (Fig. 4). Taking this spectrum as the reference one, applying the same modelling as for the X-band EPR simulation, good agreement is found. Again, the key parameters of eqn (1) Hamiltonian, controlling the EPR data profile are the Co(II) site ZFS ones and the Co(II)–Co(II) exchange interaction (Table 1), with g-tensor components less defined. The parameters found are: D = 12 cm^{-1}; $|E/D|$ = 0.14 and J_{CoCo} = −0.2 cm^{-1}, which are in line with those extracted from X-band spectrum and thus with the magnetometry DC data. In line with the X-band measurement, no information about Dy(III) site seems to be arising from HF-EPR data. One hypothesis could be that although negligible, the small Dy(III)–Co(II) interaction is hindering local Dy(III) resonances through relaxation time shortening.

AC magnetic data

To test for the dynamic of magnetization relaxation, and possible SMM behaviour we performed AC magnetometry measurements at low temperatures. Under 0 DC external applied field, magnetic susceptibility out-of-phase signal is observed below 14 K up to 10 kHz driving frequency, although no maximum is observed in the temperature dependent data profile (Fig. S12). On contrary, a clear maximum is observed in the frequency dependent data plot, with a shift with temperature (although very smooth) as expected for a thermally activated magnetization relaxation process. Only by inspection of the Cole–Cole plot a two relaxation processes profile is envisaged, although poorly resolved (Fig. 5).

Applying the generalized Debye model,[46] for a unique relaxation mode and excluding data above 5 kHz driving frequencies, the characteristic relaxation times at the different temperatures can be extracted. Attempts to fit the data with a two processes Debye model to extract the second and fastest relaxation mode, detectable only above 5 kHz driving frequencies, was unsuccessful. The small tail contaminating the Cole–Cole plot of the leading process proved insufficient to give robust relaxation times. The ln τ *vs.* T^{-1} plot for the slowest mode, evidences a linear regime at the high temperature limit, reaching an independent temperature regime at the lowest temperatures (Fig. 6). This behaviour agrees with an Orbach[47] relaxation mechanism limited by a QTM relaxation pathway dominating at lower temperatures.

$$\tau = \tau_0 e^{\frac{U_{eff}}{kT}} + \tau_{QTM} \quad (2)$$

From the data fitting through eqn (2), the following parameters are obtained for this mode: U_{eff} = 65 cm^{-1}; τ_0 = 1.1 × 10^{-5} s and τ_{QTM} = 4.5 × 10^{-3} s. On the other hand, the faster mode presumably corresponds to a different QTM temperature independent pathway.

To further explore these magnetization relaxation processes, we performed a DC external applied field scan of the AC mag-

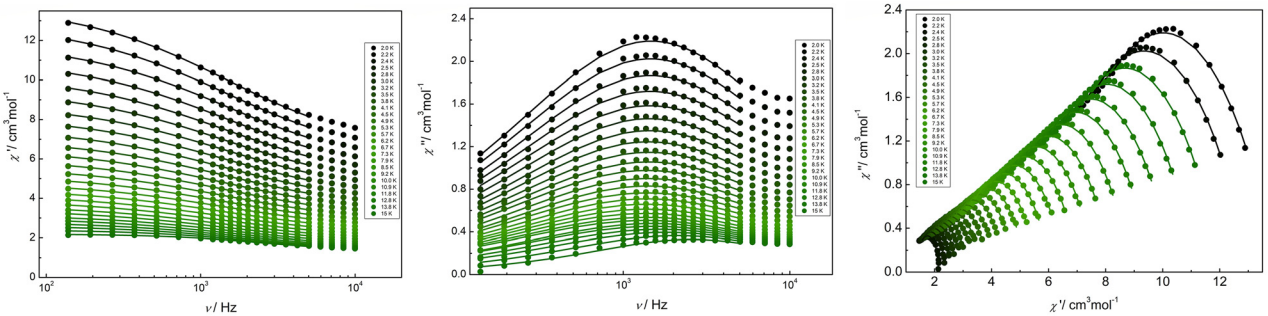

Fig. 5 Frequency dependence of the AC magnetic susceptibility data of complex **1** under 0 DC applied field below 15 K. Left: In-phase component (log scale); middle: out-of-phase component (log scale); right: Cole–Cole plot. Open symbol: experimental. Full line: simulated with best fitting parameters according to a generalized Debye model.

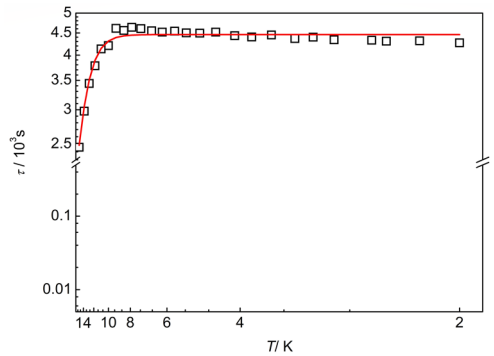

Fig. 6 τ (log scale) *vs.* T (reciprocal scale) data plot of complex **1** arising from the 0 DC AC magnetic susceptibility data. Open symbol: experimental; full line: simulated with best fitting parameters (see text).

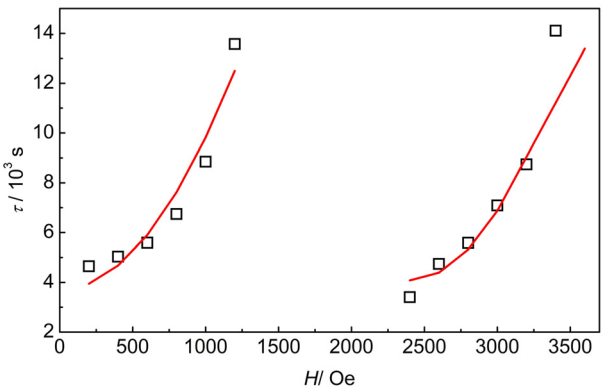

Fig. 7 τ *vs.* H data plot of complex **1** arising from the 2 K AC magnetic susceptibility data. Open symbol: experimental; full line: simulated with best fitting parameters (see text).

netic susceptibility response at 2 K (Fig. S13). In overall, the out-of-phase response decreases with increasing DC external field. Within this general behaviour, three different regimes are observed in χ'' *vs.* H data profile. Up to *ca.* 1500 Oe a strong frequency and field dependency is observed; between *ca.* 1500–2300 Oe frequency independent χ'' profile is found while for higher DC fields, although much more moderated, frequency dependency is again recovered. Above 1500 Oe the field dependency becomes smoother than in the range 0–1500 Oe. These different regimes are further corroborated when looking at the Cole–Cole plot, where the semi-circle behaviour is lost in the range *ca.* 1500–2300 Oe (Fig. S14).

At the low field and high field regimes, the characteristic relaxation times can be extracted through a single mode generalized Debye model (Fig. S15). At both fields regimes a second relaxation process is distinguished (at low fields above 5 kHz; while at high fields below 600 Hz), however due to its poor contribution, it is impossible to extract the relaxation time through a two mode Debye model. Thus, the relaxation times of the main mode were obtained excluding some frequency ranges. When looking at the relaxation times field dependence data plot profile, a clear switch of relaxation channel is observed (Fig. 7). From the relaxation time field dependency data plot, it is clear that both channels involved a QTM relaxation profile according to eqn (3):

$$\tau_{QTM} = \frac{1 + B_2 H^2}{B1} \quad (3)$$

When looking at the relaxation time at zero-field limit, the value observed for the low field channel agrees with the τ_{QTM} found from the temperature dependent AC data, in fact the best fitting parameters with eqn (3) are: $B_1 = 270\ s^{-1}$ and $B_2 = 1.6 \times 10^{-6}\ s\ Oe^{-2}$. The τ_{QTM} at zero field corresponds to B_1^{-1}, in this case τ_{QTM} (0 Oe) $= 3.7 \times 10^{-3}$ s.

Regarding the high field channel, its profile looks almost identical to the low field channel, suggesting a connection between them. If the high field channel is considered as just becoming available above *ca.* 2300 Oe, a reasonable fitting through eqn (3) is achieved with parameters essentially coincident with the low field channel ones: $B_1 = 245\ s^{-1}$ and $B_2 = 1.9 \times 10^{-6}\ s\ Oe^{-2}$.

We additionally collected AC data at DC external applied fields of 1500 Oe and 2600 Oe. At 1500 Oe a maximum at 3 K is detected in the χ'' *vs.* T plot at the different frequencies, while at 2600 Oe the maximum can be identified below 4 K.

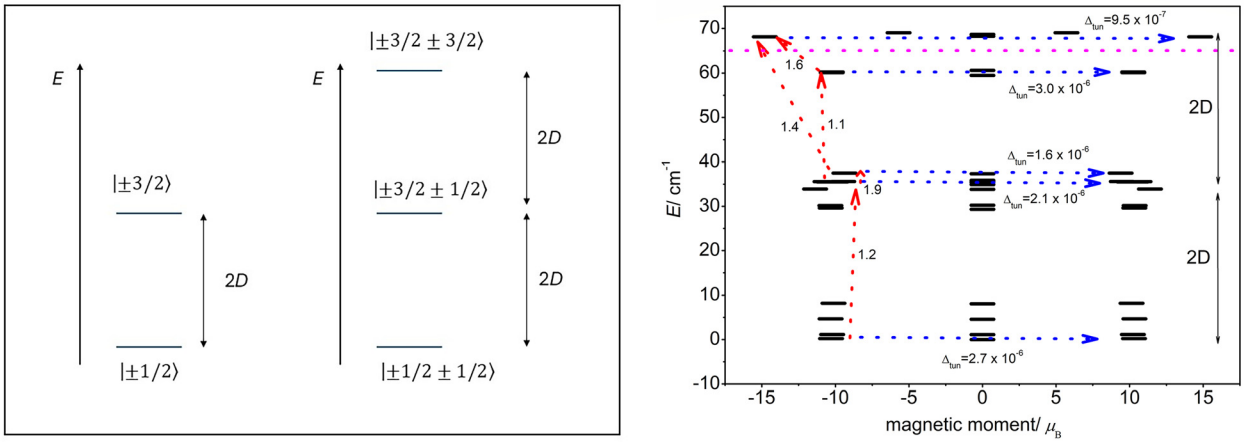

Fig. 8 Left: Thermal barrier expected for two isolated Co(II) ion with ZFS term and two weakly exchange coupled Co(II) ions with ZFS term. Right: Possible relaxation pathways (dashed arrows) arising from *ab initio* computed transition moment matrix elements of the exchange coupled system. Red: Orbach steps; blue QTM/TA-QTM pathways; violet: U_{eff} experimental value.

However, any attempt to fit these data with a generalized Debye model afforded poor quality relaxation times. The Cole–Cole plots show that at least two relaxation processes are operative (Fig. S16 & S17).

From all the AC data and considering also the DC and EPR data, together with quantum computed results, it is possible to propose a possible scheme that explains the SMM behaviour of complex **1**. Considering the magnitude of the experimentally obtained Orbach thermal barrier, no excited doublets of local Dy(III) sites can be involved, hence the relaxation barrier must be Co(II) in origin. In a simplified picture, an S = 3/2 with ZFS contribution affords a maximum barrier of $2|D|$, while two weakly coupled S = 3/2 ions must show twice this value for the U_{eff} (Fig. 8). This explanation agrees with the observed D and U_{eff} experimental magnitudes. On the other hand, if the exchange system energy spectrum is obtained through the POLY_ANISO routine (Table S2), including a J_{CoCo} = −1 cm^{-1} (the dipolar interaction contributions are negligible in comparison), then the transition moment matrix elements are available, offering a further insight into the possible relaxation pathways (Fig. 8). As in the simplified S = 3/2 model, a two-step Orbach barrier is available where each step is coincident with the $2|D|$ magnitude. Two thermally assisted QTM relaxation pathways are possible in addition to the intra-lowest magnetic state QTM route. The increased multiplicity of states arising is related to the non-coupled local Dy(III) ground KDs. Of course, the statement of uncoupled Dy(III) ions is based on the absence of experimental evidence collected so far but cannot be definitively ruled out. At least at this point, the best explanation for the magnetization relaxation behaviour in complex **1** is based on a model of two weakly coupled Co(II) sites with a sizeable ZFS contribution which is the origin of the thermal barrier. The Dy(III) ions are just passive spectators, only contributing to the total magnetic moment of the low-lying energy levels. Only a few Co(II)/Dy(III) SMM with reported magnetization relaxation parameters can be found in literature which are shown in Table 3. None of them show a Co(II) unique relaxation pathways as observed for complex **1**.

Table 3 Co(II)/Dy(III) SMM magnetization relaxation parameters

	U_{eff}/cm^{-1}	τ QTM/s	Raman	Ref.
Co^{II}_2Dy	416	7.4×10^{-2}	Yes	29
$Co^{II}_2Dy_2$	82; 11	—	—	30
$Co^{III}_2Co^{II}Dy$	60	—	Yes	32
$Co^{III}_4Co^{II}_2Dy_2$	65	4.5×10^{-3}	—	This work
$Co^{II}_2Dy_{10}$	17; 3	—	—	31

Conclusions

We have successfully isolated and structurally characterized by single crystal X-ray diffraction measurements the first example of a Co/Dy heterometallic complex with the $\{Co^{III}_4Co^{II}_2Dy_2\}$ motif where the molecular structure can be described as two connected equivalent asymmetric butterfly $\{Co^{III}_2Co^{II}Dy^{III}\}$ cores bridged through carboxylate and alkoxide bridges. The DC magnetometry and the EPR experimental data can be understood with a simple spin Hamiltonian considering two S = 3/2 with moderate ZFS contribution (positive D parameter *ca.* 12–20 cm^{-1}) with a weak anti-ferromagnetic exchange interaction (J *ca.* −1 cm^{-1}). This implies a weak Co(II)–Co(II) exchange interaction with negligible or not detectable Co(II)–Dy(III) interactions. From here it follows that the Dy(III) sites play primarily a spectator role based on current evidence, contributing just with the high magnetic moment of their ground KD.

In addition, the Orbach thermal barrier arising from the 0 DC AC data is compatible with two weakly coupled Co(II) ions with a sizeable D parameter. Within this scheme, the U_{eff} value is close to $4D$ which is the expected magnitude. Quantum computed low-lying energy levels of the local Dy(III) site, show that

the first excited KD is at *ca.* 140 cm^{-1}, too high to be related to the observed thermal barrier. Thus, the SMM behaviour is based on Co(II) sites with uncoupled Dy(III) ground KDs. Of course that more studies are necessary to definitely assess the real magnitude of the Co(II)–Dy(III) exchange and hence confirm the precise role of Dy(III) sites in the SMM response of complex **1**.

Experimental section

Material and physical measurements

All chemicals were reagent grade and used as received without further purification. Dysprosium nitrate was prepared by stoichiometric reaction of the oxide with aqueous nitric acid. Elemental analysis for C, H and N was performed with a Carlo Erba 1108 analyzer. Magnetic measurements were performed with a Quantum Design Dynacool Physical Properties Measurement System (PPMS), equipped with a Vibrating Sample Magnetometer (VSM). All experimental magnetic data were corrected for the diamagnetism of the sample holders and of the constituent atoms ($M_w/2 \times 10^{-6}$ cm^3 mol^{-1} approximation). DC measurements were conducted from 1.8 to 300 K at 1 kOe and between 1.8–10 K in the range 1–90 kOe. AC measurements were performed with driving fields between 3–6 Oe and frequencies up to 10 kHz. Thermogravimetric analyses were performed on a Mettler Toledo TGA/DSC-II system. The sample was introduced in an alumina holder and heated under an air atmosphere from room temperature to 900 °C with a heating rate of 10 °C min^{-1}. Powder X-ray diffractograms were collected on a Panalytical Empyrean Powder Diffractometer using Cu radiation, Kα1 = 1.54 Å and equipped with a PIXcel3D area detector, in the range of 4 to 40 degrees in $\theta/2\theta$ configuration, with a step of 0.026 degrees. The equipment was calibrated with a silicon standard. For the determination, the sample was pulverized in mortar and seeded on a zero-background silicon sample holder.

Preparation of complex $[Co^{III}_4Co^{II}_2Dy^{III}_2(tea)_4(CH_3COO)_4(OH)_2(NO_3)_4]\cdot 2H_2O$ (1)

$Co(NO_3)_2\cdot 6H_2O$ (59.6 mg, 0.2 mmol), $Dy(NO_3)_3\cdot xH_2O$ (35.1 mg, 0.1 mmol) and acetic acid (45 μL, 0.8 mmol) were dissolved in 10 mL of acetonitrile under constant stirring (solution A). Separately, triethanolamine (0.2 mmol, from a 1 M solution in acetonitrile) and triethylamine (83 μL, 0.6 mmol) were mixed in 5 mL of acetonitrile (solution B). Solution B was added dropwise to solution A under continuous stirring at room temperature. The reaction mixture was further stirred for 1 hour, resulting in the formation of a pink solution. The mixture was filtered to remove any insoluble materials and left sealed standing. After 4 months, good shape single crystals appeared. They were filtered, washed with acetonitrile and air dried. Yield: 0.047 g, 26% (Dy based). Anal. calcd for $C_{32}H_{66}Co_6Dy_2N_8O_{36}$ (1817.50 g mol^{-1}) C: 21.1, H: 3.7 N: 6.2 found: C: 21.8, H: 4.0, N: 5.4.

X-ray structure determination

Crystal structure of the reported complex was determined with an Oxford Xcalibur, Eos, Gemini CCD area-detector diffractometer using graphite-monochromated Mo-Kα radiation (λ = 0.71069 Å) at 298 K. Crystals were directly obtained from the synthetic procedure. Data was corrected for absorption with CrysAlisPro, Oxford Diffraction Ltd, version 1.171.33.66, applying an empirical absorption correction using spherical harmonics, implemented in SCALE3 ABSPACK scaling algorithm.[48] The structures were solved by direct methods with SHELXT[49] and refined by full-matrix least-squares on F^2 with SHELXL-2014[50] under WinGX platform.[51] Hydrogen atoms were added geometrically and refined as riding atoms with a uniform value of U_{iso}, except for hydroxo ligands, whose hydrogen atoms were located in the electron density difference map and further refined as riding atoms with fixed U_{iso} = 1.5U_{iso}(O). One of the tea^{3-} ligand in the asymmetric unit shows a disordered methylene group which was refined around two split positions with equal occupation numbers. Final crystallographic data and values of R_1 and wR are listed in Table S1. CCDC 2454417 contains the supplementary crystallographic data for this paper.

X-band and high field EPR measurements

X-band EPR measurements were carried out on a Bruker EMX spectrometer, equipped with and Oxford 4102ST cryostat. Samples were prepared in quartz glass tubes and measured in the standard TE102 cavity. High-frequency EPR spectra of pressed powder samples (180–350 GHz) were recorded on a home-built spectrometer. Its radiation source is an 8–20 GHz signal generator (VDI) in combination with an amplifier–multiplier chain (VDI) to obtain the required frequencies. It features a quasi-optical bridge (Thomas Keating) and induction mode detection. The detector is a QMC magnetically tuned InSb hot electron bolometer. The sample is located in an Oxford Instruments 15/17 T cryomagnet equipped with a variable temperature insert (1.5–300 K). The simulations were carried out using the PHI package.

Quantum chemical calculations

All computations were carried out with the ORCA 5.0 program package.[52] For the computation of the exchange interaction J parameter single point calculations for the high-spin state (HS) and the broken symmetry states (BS) at the X-ray geometry were carried out at the B3LYP level of DFT, incorporating the relativistic effect by means of the zeroth-order regular approximation (ZORA) and employing the ZORA-def2-TZVP Ahlrichs basis set for all atoms except for Dy atom for which the SARC-ZORA-TZVP basis set was chosen. Taking advantage of the RI (Resolution of Identity) approximation, SCF calculations were of the spin-polarized type and were tightly converged ($10^{-7}E_h$ in energy, 10^{-6} in the density change and 10^{-6} in maximum element of the DIIS error vector).

The methodology applied here relies on the broken symmetry formalism, originally developed by Noodleman for SCF

methods,[53] which involves a variational treatment within the restrictions of a single spin-unrestricted Slater determinant built upon using different orbitals for different spin. This approach has been later applied within the frame of DFT.[54] The HS (high spin) and BS (broken symmetry) energies were then combined to estimate the exchange coupling parameter J involved in the widespread used Heisenberg–Dirac–van Vleck Hamiltonian. We used the method proposed by Ruiz and co-workers,[55] where the following equation is applied:

$$E_{BS} - E_{HS} = 2J_{12}(2S_1S_2 + S_2), \quad \text{with } S_2 < S_1. \qquad (4)$$

We have calculated the different spin topologies of broken symmetry nature by alternatively flipping spin on the different metal sites (Table S5). The exchange coupling constants J_i were obtained after considering the individual pair-like components spin interactions involved in the description of the different broken symmetry states by solving a set of linear equations.

For describing the single ion Co(II) site and Dy(III) site magnetic properties, we performed computations at the complete active space self-consistent field (CASSCF) level, with a state averaged (SA) spin–orbit coupling (SOC) approach. The other Co(II) and Dy(III) sites were replaced by Zn(II) and Y(III) ions. We computed the full d^7 microstates, 10 quartets and 40 doublets for the high spin Co(II) ion while in the case of Dy(III) site we computed the 21 sextets. For the SOC-SA-CASSCF calculation, the active space contained 7 electrons in 5 orbitals (the five 3d orbitals) for Co(II); and 9 electrons in 7 orbitals (the seven 4f orbitals) for Dy(III). We incorporated the relativistic effect by means of the DKH approximation employing the DKH-def2-SVP basis set for all atoms except for metal atoms for which the following basis set were chosen: DKH-def2-TZVP (Co, Zn); SARC-DKH-TZVP (Y) and SARC2-DKH-QZVP (Dy). The calculations utilized the RI approximation. For the treatment of the spin–orbit coupling (SOC), an approximation to the Breit–Pauli form of the spin–orbit coupling operator (SOMF) was employed. Final ZFS parameters, g tensors, main magnetic axes and energies were obtained through the SINGLE-ANISO module.

For computing the magnetic properties of the exchange picture in complex **1**, the POLY_ANISO module was employed, which uses the previously calculated local properties derived from the SINGLE_ANISO code. It uses an approach combining the calculated electronic and magnetic properties of individual metal fragments with the model description of the anisotropic exchange interaction between metal sites, achieved within the Lines model.[43,44]

In this model, the isotropic Heisenberg exchange interaction is included between the true spins on neighbouring metal sites (S = 3/2 for Co(II) and S = 5/2 for Dy(III)) in the absence of spin–orbit coupling.

Conflicts of interest

There are no conflicts of interest to declare.

Data availability

The data supporting this article have been included as part of the supplementary information (SI). Supplementary information is available. See DOI: **https://doi.org/10.1039/d5dt01689d**.

CCDC 2454417 contains the supplementary crystallographic data for this paper.[56]

Acknowledgements

We gratefully acknowledge Universidad de Buenos Aires, Agencia Nacional de Promoción Científica y Tecnológica and Consejo Nacional de Investigaciones Científicas y Técnicas for funding resources. PA is a staff member of CONICET, LM is a doctoral fellowship of CONICET. The authors gratefully acknowledge the computing time granted on the supercomputer Mogon at Johannes Gutenberg University Mainz (hpc.uni-mainz.de) and the FAIRE programme provided by the Cambridge Crystallographic Data Centre (CCDC) for the opportunity to use the Cambridge Structural Database (CSD) and associated software. VPG acknowledges, CONICYT-FONDEQUIP/PPMS/EQM130086-UNAB, Fondo Nacional de Desarrollo Científico y Tecnológico 1252136, and CEDENNA. CC acknowledges ANID Fondo Nacional de Desarrollo Científico y Tecnológico iniciación no. 11241257. Authors also deeply acknowledge Maricel Rodriguez for the pXRD data collection.

References

1 D. Gatteschi, R. Sessoli and J. Villain, *Molecular Nanomagnets*, Oxford University Press, 2006.
2 M. J. Giansiracusa, G. K. Gransbury, N. F. Chilton and D. P. Mills, in *Encyclopedia of Inorganic and Bioinorganic Chemistry*, ed. R. A. Scott, Wiley, 2nd edn, 2021, pp. 1–21.
3 M. Affronte, *J. Mater. Chem.*, 2009, **19**, 1731–1737.
4 F. Troiani and M. Affronte, *Chem. Soc. Rev.*, 2011, **40**, 3119–3129.
5 R. Sessoli, *Angew. Chem., Int. Ed.*, 2012, **51**, 43–45.
6 M. R. Wasielewski, M. D. E. Forbes, N. L. Frank, K. Kowalski, G. D. Scholes, J. Yuen-Zhou, M. A. Baldo, D. E. Freedman, R. H. Goldsmith, T. Goodson, M. L. Kirk, J. K. McCusker, J. P. Ogilvie, D. A. Shultz, S. Stoll and K. B. Whaley, *Nat. Rev. Chem.*, 2020, 1–15.
7 L. Bogani and W. Wernsdorfer, *Nat. Mater.*, 2008, **7**, 179–186.
8 X.-L. Li, F.-Y. Min, C. Wang, S.-Y. Lin, Z. Liu and J. Tang, *Inorg. Chem.*, 2015, **54**, 4337–4344.
9 L. Rosado Piquer and E. C. Sañudo, *Dalton Trans.*, 2015, **44**, 8771–8780.
10 S. K. Langley, D. P. Wielechowski, V. Vieru, N. F. Chilton, B. Moubaraki, B. F. Abrahams, L. F. Chibotaru and K. S. Murray, *Angew. Chem., Int. Ed.*, 2013, **52**, 12014–12019.
11 T. Gupta, M. F. Beg and G. Rajaraman, *Inorg. Chem.*, 2016, **55**, 11201–11215.

12 S. K. Singh, M. F. Beg and G. Rajaraman, *Chem. – Eur. J.*, 2016, **22**, 672–680.
13 J. Li, R.-M. Wei, T.-C. Pu, F. Cao, L. Yang, Y. Han, Y.-Q. Zhang, J.-L. Zuo and Y. Song, *Inorg. Chem. Front.*, 2017, **4**, 114–122.
14 B.-K. Ling, Y.-Q. Zhai, P.-B. Jin, H.-F. Ding, X.-F. Zhang, Y. Lv, Z. Fu, J. Deng, M. Schulze, W. Wernsdorfer and Y.-Z. Zheng, *Matter*, 2022, **5**, 3485–3498.
15 P. Shukla, M. Ezhava, S. Roy, A. Mallick and S. Das, in *Tailored Functional Materials*, ed. K. Mukherjee, R. K. Layek and D. De, Springer Nature Singapore, Singapore, 2022, vol. 15, pp. 199–208.
16 M. Murrie, *Chem. Soc. Rev.*, 2010, **39**, 1986.
17 S. Tripathi, A. Dey, M. Shanmugam, R. S. Narayanan and V. Chandrasekhar, in *Organometallic Magnets*, ed. V. Chandrasekhar and F. Pointillart, Springer International Publishing, Cham, 2019, pp. 35–75.
18 P. Kumar Sahu, R. Kharel, S. Shome, S. Goswami and S. Konar, *Coord. Chem. Rev.*, 2023, **475**, 214871.
19 P. Zhang, Y.-N. Guo and J. Tang, *Coord. Chem. Rev.*, 2013, **257**, 1728–1763.
20 C. Benelli and D. Gatteschi, *Introduction to Molecular Magnetism: From Transition Metals to Lanthanides*, Wiley, 1st edn, 2015.
21 S. K. Langley, D. P. Wielechowski, B. Moubaraki and K. S. Murray, *Chem. Commun.*, 2016, **52**, 10976–10979.
22 J. H. Mecchia Ortiz, D. Cabrosi, L. M. Carrella, E. Rentschler and P. Alborés, *Chem. – Eur. J.*, 2022, **28**, e202201450.
23 D. Chauhan, K. R. Vignesh, A. Swain, S. K. Langley, K. S. Murray, M. Shanmugam and G. Rajaraman, *Cryst. Growth Des.*, 2023, **23**, 197–206.
24 A. Zabala-Lekuona, A. Landart-Gereka, M. M. Quesada-Moreno, A. J. Mota, I. F. Díaz-Ortega, H. Nojiri, J. Krzystek, J. M. Seco and E. Colacio, *Inorg. Chem.*, 2023, **62**, 20030–20041.
25 R. Ruamps, R. Maurice, C. De Graaf and N. Guihéry, *Inorg. Chem.*, 2014, **53**, 4508–4516.
26 L. Ungur, M. Thewissen, J.-P. Costes, W. Wernsdorfer and L. F. Chibotaru, *Inorg. Chem.*, 2013, **52**, 6328–6337.
27 J. Cirera, E. Ruiz, S. Alvarez, F. Neese and J. Kortus, *Chem. – Eur. J.*, 2009, **15**, 4078–4087.
28 D. Basak, J. V. Leusen, T. Gupta, P. Kögerler, V. Bertolasi and D. Ray, *Inorg. Chem.*, 2020, **59**, 2387–2405.
29 J.-L. Liu, J.-Y. Wu, G.-Z. Huang, Y.-C. Chen, J.-H. Jia, L. Ungur, L. F. Chibotaru, X.-M. Chen and M.-L. Tong, *Sci. Rep.*, 2015, **5**, 16621.
30 K. C. Mondal, A. Sundt, Y. Lan, G. E. Kostakis, O. Waldmann, L. Ungur, L. F. Chibotaru, C. E. Anson and A. K. Powell, *Angew. Chem., Int. Ed.*, 2012, **51**, 7550–7554.
31 L.-F. Zou, L. Zhao, Y.-N. Guo, G.-M. Yu, Y. Guo, J. Tang and Y.-H. Li, *Chem. Commun.*, 2011, **47**, 8659.
32 W.-N. Li, C.-F. Yu, J.-R. Jiang, Y. Zhou, Y.-J. Zhu, X.-P. Zhao and H.-S. Wang, *Polyhedron*, 2025, **268**, 117390.
33 H. Xiang, Y. Lan, H.-Y. Li, L. Jiang, T.-B. Lu, C. E. Anson and A. K. Powell, *Dalton Trans.*, 2010, **39**, 4737.
34 A. V. Funes, M. Perfetti, M. Kern, N. Rußegger, L. Carrella, E. Rentschler, J. Slageren and P. Alborés, *Eur. J. Inorg. Chem.*, 2021, **2021**, 3191–3210.
35 C. Sarto, M. Rouzières, J.-L. Liu, H. Bamberger, J. van Slageren, R. Clérac and P. Alborés, *Dalton Trans.*, 2018, **47**, 17055–17066.
36 A. V. Funes, L. Carrella, Y. Rechkemmer, J. van Slageren, E. Rentschler and P. Alborés, *Dalton Trans.*, 2017, **46**, 3400–3409.
37 A. V. Funes, L. Carrella, E. Rentschler and P. Alborés, *Chem. – Eur. J.*, 2016, **22**, 14308–14318.
38 A. V. Funes, L. Carrella, L. Sorace, E. Rentschler and P. Alborés, *Dalton Trans.*, 2015, **44**, 2390–2400.
39 A. V. Funes, L. Carrella, E. Rentschler and P. Alborés, *Dalton Trans.*, 2014, **43**, 2361–2364.
40 X.-Q. Zhao, J. Wang, D.-X. Bao, S. Xiang, Y.-J. Liu and Y.-C. Li, *Dalton Trans.*, 2017, **46**, 2196–2203.
41 X. Zhao, T. Zhao, Y. Wang and J. Zhou, *Appl. Organomet. Chem.*, 2023, **37**, e7104.
42 S. Alvarez, P. Alemany, D. Casanova, J. Cirera, M. Llunell and D. Avnir, *Coord. Chem. Rev.*, 2005, **249**, 1693–1708.
43 M. E. Lines, *J. Chem. Phys.*, 1971, **55**, 2977–2984.
44 L. F. Chibotaru, L. Ungur, C. Aronica, H. Elmoll, G. Pilet and D. Luneau, *J. Am. Chem. Soc.*, 2008, **130**, 12445–12455.
45 N. F. Chilton, R. P. Anderson, L. D. Turner, A. Soncini and K. S. Murray, *J. Comput. Chem.*, 2013, **34**, 1164–1175.
46 K. S. Cole and R. H. Cole, *J. Chem. Phys.*, 1941, **9**, 341–351.
47 R. Orbach, *Proc. R. Soc. London, Ser. A*, 1961, **264**, 458–484.
48 *SCALE3 ABSPACK: Empirical absorption correction, CrysAlis – Software package*, 2006.
49 G. M. Sheldrick, *Acta Crystallogr., Sect. A: Found. Adv.*, 2015, **71**, 3–8.
50 G. M. Sheldrick, *Acta Crystallogr., Sect. A: Found. Adv.*, 2008, **64**, 112–122.
51 L. J. Farrugia, *J. Appl. Crystallogr.*, 2012, **45**, 849–854.
52 F. Neese, *Wiley Interdiscip. Rev.: Comput. Mol. Sci.*, 2012, **2**, 73–78.
53 L. Noodleman, *J. Chem. Phys.*, 1981, **74**, 5737–5743.
54 L. Noodleman and E. J. Baerends, *J. Am. Chem. Soc.*, 1984, **106**, 2316–2327.
55 E. Ruiz, J. Cano, S. Alvarez and P. Alemany, *J. Comput. Chem.*, 1999, **20**, 1391–1400.
56 CCDC 2454417: Experimental Crystal Structure Determination, 2025, DOI: **10.5517/ccdc.csd.cc2nd0rv**.